Ore Geology Reviews 91 (2017) 477–490

Contents lists available at ScienceDirect

Ore Geology Reviews

journal homepage: www.elsevier.com/locate/oregeorev

Trace element geochemistry of magnetite from the giant Beiya gold-polymetallic deposit in Yunnan Province, Southwest China and its implications for the ore forming processes

Xiaoming Sun[a,b,c,*], Hai Lin[a,b], Yu Fu[a,b,*], Dengfeng Li[a,b], Pete Hollings[d], Tianjian Yang[b,c], Zhangrong Liu[e]

[a] School of Marine Sciences, Sun Yat-sen University, Guangzhou 510006, China
[b] Guangdong Provincial Key Laboratory of Marine Resources and Coastal Engineering, Guangzhou 510275, China
[c] School of Earth Sciences and Engineering, Sun Yat-sen University, Guangzhou 510275, China
[d] Department of Geology, Lakehead University, 955 Oliver Road, Thunder Bay, Ontario P7B 5E1, Canada
[e] Yunnan Gold and Mineral Group Co. Ltd, Kunming 650224, China

ARTICLE INFO

Keywords:
Magnetite
Trace element geochemistry
Beiya giant deposit
Skarn
Ore forming process

ABSTRACT

The Beiya gold–polymetallic deposit is one of the largest gold deposits in China and is considered to be a typical porphyry-skarn system located in the middle of the Jinshajiang–Ailaoshan alkaline porphyry metallogenic belt. Massive magnetite is widespread in the Beiya ore district but its genesis is still the subject of debate. Five representative magnetite types are present in the Beiya deposit, namely magmatic magnetite (M1) from the ore-related porphyry, disseminated magnetite (M2) from the early retrograde alteration, massive magnetite (M3) from the early quartz-magnetite stage, massive magnetite (M4) from the middle quartz-magnetite stage and magnetite (M5) from the late quartz-magnetite stage. Compared with the M1 magnetite, the magnetites from stages M2 to M5 are depleted in Ti, Al and high field strength elements, implying a hydrothermal origin, distinct from the magmatic accessory magnetite in the ore-related porphyry (M1). The concentrations of cobalt in the hydrothermal magnetites decrease gradually from M2 to M5, and can be used to discriminate the magnetite types. The Al + Mn and Ti + V contents of the successively precipitated magnetite grains (M2–M5) suggests that the ore forming temperature decreased from M2 to M4, but increased from M4 to M5, possibly as the result of a new pulse of magma entering the chamber, which may have triggered the gold mineralization. The V content in the hydrothermal magnetite suggests that the oxygen fugacity increased from M2 to M4 but decreased as soon as the sulfides entered the system (M5).

1. Introduction

The giant Beiya gold–polymetallic deposit lies in the middle of the Jinshajiang-Ailaoshan alkaline porphyry metallogenic belt and is the largest skarn gold deposit in China with estimated reserves of 130.8 million tonnes (Mt) of Au (average grade: 2.47 g/t), 170 Mt of Fe (average grade: 33.3 wt%), 125 Mt of Cu (average grade: 0.52 wt%), along with considerable amounts of Pb, Zn and Ag (He et al., 2016; Mao et al., 2017). Research into the ore geology, fluid geochemistry and ore genesis of the Beiya deposit suggests that the mineralization and alteration are similar to gold skarn deposits related to porphyry-skarn systems worldwide (Deng et al., 2015; Fu et al., 2017; He et al., 2015; Liu et al., 2015; Meinert et al., 2003). At Beiya, large volumes of magnetite host the Au and played an important role during gold transportation and precipitation (Zhou et al., 2016). Previous (nano-) mineralogy studies of magnetite in the Beiya deposit has provided significant insights into the evolution and physicochemical conditions of the gold polymetallic ore-forming system and suggests that there were at least two episodes of Au scavenging in magnetite by Bi melts (Tooth et al., 2011), leading to significant Au enrichment (Zhou et al., 2016). However, the geochemistry of the magnetite remains poorly understood.

Magnetite is a common accessory mineral and forms over a wide range of geologic conditions (sedimentary, magmatic or hydrothermal) and can incorporate various trace elements in its cubic spinel structure (Dare et al., 2014; Dupuis and Beaudoin, 2011; Nadoll et al., 2012). *In-situ* magnetite analysis and comparison between magmatic and hydrothermal magnetite provides a better understanding of the ore-forming

* Corresponding authors at: School of Marine Sciences, Sun Yat-sen University, Guangzhou 510006, China.
E-mail addresses: eessxm@mail.sysu.edu.cn (X. Sun), fuyu26@mail.sysu.edu.cn (Y. Fu).

http://dx.doi.org/10.1016/j.oregeorev.2017.09.007
Received 3 April 2017; Received in revised form 1 September 2017; Accepted 11 September 2017
Available online 12 September 2017
0169-1368/

fluids during the transition from magmatic to hydrothermal processes, helps to reveal the trigger(s) for magnetite precipitation and discriminates ore deposit types (Acosta-Góngora et al., 2014; Canil et al., 2016; Chen et al., 2015b; Chung et al., 2015; Dare et al., 2014, 2012; Dupuis and Beaudoin, 2011; Nadoll et al., 2014, 2012; Nadoll and Koenig, 2011).

The origin of magnetite at Beiya is still the subject of debate. Xu et al. (2007) proposed that magmatic Fe-rich fluids in Beiya formed a large number of magmatic-type Fe orebodies, whereas Li et al. (2016) proposed that there were four stages of mineralization in Beiya all of which were hydrothermal. Alternatively, He et al. (2015) suggested that the primary ore zone in Beiya is the Au-Fe-Cu segment at Wandongshan with massive sulfide and magnetite ores, which is interpreted to be of skarn origin. In this contribution, we use detailed petrographic descriptions and LA-ICP-MS trace element data for the Beiya magnetite, to investigate the petrogenesis of the magnetite and the nature of the ore forming fluids to provide direct constraints on the physicochemical conditions for the evolution of the gold polymetallic ore forming fluid in the Beiya deposit.

2. Geological setting and ore Geology

2.1. Geological setting

The Beiya gold–polymetallic deposit is situated to the east of the Jinshajiang suture (which forms the boundary of the western Yangtze Plate) approximately 90 km north of Dali in western Yunnan, SW China (Fig. 1). It is the largest gold deposit in the region and contains significant amounts of Fe, Cu, Pb, Zn and Ag. The deposit lies in the middle of the Jinshajiang-Ailaoshan alkaline porphyry metallogenic belt (Mao et al., 2014) and is made up of six ore segments: the Weiganpo, Bijiashan and Guogaishan segments in the east and the Wandongshan, Hongnitang and Jingouba segments in the west (Fig. 2a). Of these segments, the Wandongshan (mainly the KT52 ore body) is the biggest, containing most of the resources (99 Mt @2.61g/t Au; Deng et al., 2015) and is currently being mined for gold and iron. The exposed rocks in the Beiya deposit comprises the Lower Triassic Qingtianbao Formation (175–350 m), the Middle Triassic Beiya Formation and Quaternary sedimentary rocks. The Lower Triassic Qingtianbao Formation contains arkose, hornfelsed greywacke and sandstone with basaltic volcaniclastic rocks, whereas the Middle Triassic Beiya Formation contains dolomitic, ferruginous, bioclastic and argillaceous limestones (*ca.* 138–531 m, the main ore-bearing host rock). The strata occur in a N–trending basin upon which is superimposed a broad N-S syncline (He et al., 2015). The igneous suites in and around the ore district includes the Upper Permian Emeishan Formation basalt and the regionally widespread Cenozoic alkaline porphyries. The Emeishan Formation is found in the southeastern part of the mining area, with basalt being the major rock type. The regionally widespread Cenozoic alkaline porphyries include (quartz) syenite-, biotite-K-feldspar- and quartz-albite porphyries (He et al., 2015; Liu et al., 2015; Xu et al., 2007, 2006; Xue et al., 2008) are relatively rare in the district but are closely related to the mineralization in the Beiya deposit.

Two main fault systems are present in the district, striking north and east, of which the approximately N-striking ones are dominant, such as the Maanshan Fault (a branch of the Jinshajiang-Honghe strike-slip fault system; Li et al., 2016). This fault extends across western Beiya, and the associated secondary structures are interpreted to control the porphyry/orebody emplacement in the Wandongshan and Hongnitang ore segments (Li et al., 2016). The E-striking fault system likely formed after the mineralization at Beiya and probably destroyed some ore bodies (He, 2014).

2.2. Ore deposit Geology

The ore bodies at Beiya mostly occur in and/or along the contact zones between intrusions and the carbonate host rocks of the Beiya Formation. Some stratiform orebodies are locally distributed along flat interlayer fractures and breccia zones within the Beiya Formation carbonates, as well as at the contact of the carbonates and the underlying Qingtianbao Formation sandstone. Vein-like orebodies occur within the porphyritic intrusions, and laterite-hosted orebodies have also been documented (Li et al., 2016). Based on previous studies, the mineralization style at Beiya can be divided into porphyry, skarn and supergene styles (Zhou et al., 2016). Of these, skarn is the major mineralization type at Beiya, with orebodies mostly found along the intrusive contact between porphyries and the Beiya Formation carbonates. Orebody KT52 (around the Wandongshan porphyry) is the largest skarn orebody (Fig. 2b), with proven reserves of 87.2 Mt Au @ 2.35 g/t, along with 90.27 Mt Fe @ 34 wt%, and 111.8 Mt Cu @ 0.34 wt% (Li et al., 2016).

The dominant skarn mineralization comprises three stages (Fig. 3): (1) skarn, (2) retrograde alteration (including quartz-magnetite stage) and (3) hydrothermal quartz-sulfide stages. Minerals in skarn stage are mainly anhydrous, such as garnet (Fig. 4a) and pyroxene, whereas retrograde alteration minerals are predominantly hydrous, including epidote-group minerals, biotite and chlorite. Magnetite, titanite, scheelite, feldspar (including plagioclase and albite) and fluorite can also be found in the retrograde alteration stage. Magnetite mineralization mainly formed during the late retrograde alteration stage (quartz-magnetite stage) and locally occurs as abundant massive magnetite. The hydrothermal quartz-sulfide stage is characterized by pyrite, chalcopyrite, pyrrhotite and molybdenite, both the magnetite and sulfide stages are associated with the gold mineralization. The secondary enriched oxide orebodies with gold-bearing hematite and limonite can be found along the unconformity between the Beiya Formation and the overlying Quaternary sediments, which are interpreted to be the weathering and leaching products of primary sulfides and magnetite. The paragenesis has been constrained by detailed geochronological studies of the different ore forming stages. The porphyries emplaced at Beiya include the quartz syenite porphyry, the quartz monzonite porphyry, the biotite orthoclase porphyry, the quartz albite porphyry and a group of lamprophyre dikes. Most of them were emplaced at around 36.9–33.3 Ma (Deng et al., 2015; Fu et al., 2015; He et al., 2015, 2013, 2012; Jiang et al., 2013; Liu et al., 2015; Lu et al., 2012; Xu, 2007), except for the quartz albite porphyry (65 Ma) and the biotite orthoclase porphyry (3.8 Ma) (Xu et al., 2007). The quartz syenite porphyry at Beiya has yielded a (LA-ICP-MS) U-Pb zircon age of 36.07 ± 0.43 Ma (Fu et al., 2015), which indicates that the skarn did not occur before ~36.07 Ma. Hydrothermal titanite from the retrograde alteration stage yielded a weighted average $^{206}Pb/^{238}U$ age of 33.1 ± 1.0 Ma, representing the age of the retrograde alteration and the maximum age for the gold precipitation (Fu et al., 2016). Molybdenite from Beiya has yielded an isochron age of 34.7 ± 1.6 Ma, which constrains the age of the quartz-sulfide stage (Fu et al., 2015). Even though the age of hydrothermal titanite and molybdenite overlap within error, the magnetite from the retrograde alteration stage formed slightly earlier than the sulfide, as the magnetite is locally cut by the pyrite veins (Fig. 4b).

At Beiya, gold mainly occurs as native gold and electrum in cracks and/or as vein-fill with pyrite, magnetite, limonite and quartz. During the retrograde alteration (quartz-magnetite) stage and quartz-sulfide stage, gold can be hosted by magnetite and sulfides (pyrite, chalcopyrite, and bismuthinite) respectively. In the massive magnetite ores, abundant native gold was observed as submicron-scale inclusions hosted by magnetite, and chemical analyses of separated minerals in the Beiya Au ores show that magnetite hosts at least 14% of the total Au resources (Zhou et al., 2017). The ore forming process may involve at least two episodes of Au scavenging by Bi-bearing melts, leading to significant Au enrichment (Zhou et al., 2016). The compositions of the Beiya skarn minerals suggest a typical oxidized skarn system (He et al., 2015). Studies of fluid inclusions indicate moderate to high temperatures (186–372 °C) and high salinities (7.5–19.8 wt% NaCl equiv.) for

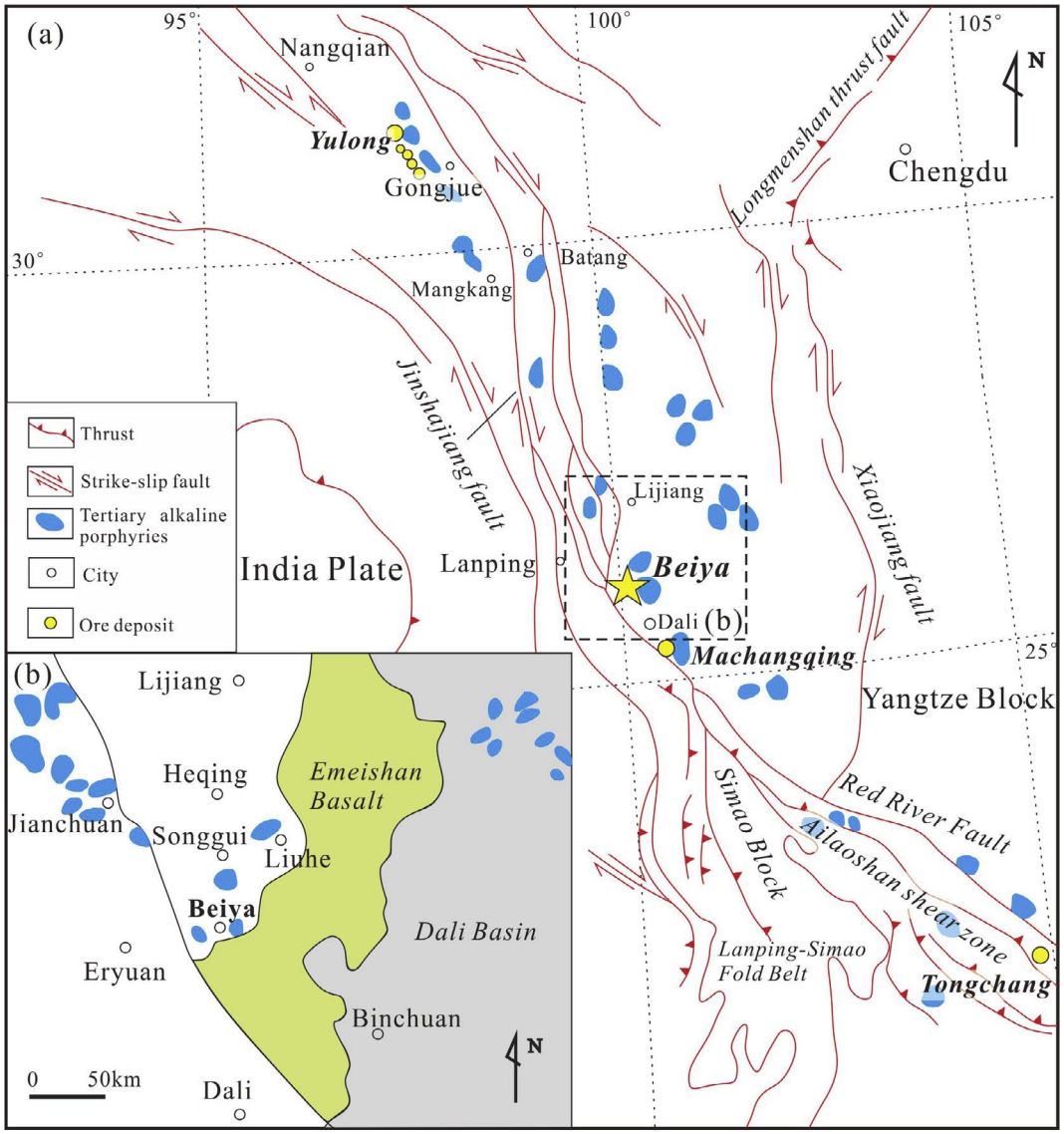

Fig. 1. Tectonic setting of the Beiya area (Modified after Wang et al., 2001).

the metallogenic fluids, which likely originated from the magma with late-stage meteoric water involvement (He, 2014). The sulfur isotope signature of the sulfide mineralization stage ranges from –2.4 to 4.5‰, suggesting that the ore fluid was derived from, and/or modified by the magma (He, 2014; Li et al., 2016; Xiao et al., 2011). The $\delta^{18}O$ and δD compositions of the ore-forming fluids in the quartz-sulfide stage are –0.85 to 3.52‰ and –78.6 to –88.6‰, respectively (He, 2014). The isotope evidence suggests that the ore-forming materials of the Beiya deposit were derived from deep-sourced magmas (He, 2014; Li et al., 2016).

3. Sampling and analytical methods

Magnetite samples for in-situ element analysis were all collected from the Wandongshan ore segment. Sample W007 (M1; Fig. 4c) is ore-related quartz syenite porphyry collected from the open pit. The porphyry is light gray and consists of K-feldspar (50 vol%), quartz (30 vol %) and plagioclase (10 vol%), with accessory zircon, apatite, titanite and magnetite. Sample W364 (M2; Fig. 4d) was from drill hole 84ZK11 in the early retrograde alteration and contains disseminated magnetite and feldspar, local pyroxene and quartz, and trace titanite and allanite. Sample W009 (M3; Fig. 4e) was collected from Fe-oxide ores in the open pit and comprises massive magnetite (> 80 vol%) with silicate gangue minerals such as epidote and chlorite, representing the early quartz-magnetite stage. Sample W566 (M4; Fig. 4f) was collected from Fe-oxide ores at the contact between the intrusion and country rock in hole 52ZK7 and represents the middle quartz-magnetite stage, which consists of massive magnetite (~70 vol%) and minor sulfides (< 30 vol %) including chalcopyrite and pyrite. Sample W561 (sulfide ore; Fig.4g) is a sulfide-dominated vein within altered country rock, with minor magnetite (< 10 vol%) in the sulfides. It was collected from drill hole 52ZK4 and the magnetite (M5) in it probably formed in the late quartz-magnetite stage and was mostly altered by the sulfides in the subsequent quartz-sulfide stage.

All samples were prepared as polished thin sections with a thickness of ~ 50 μm and subsequently examined using an optical microscope and Back-Scattered Electron (BSE) imaging to characterize the mineralogy and texture of magnetite. The BSE images of magnetite were obtained with a Zeiss SIGMA field-emission Scanning Electron Microprobe (SEM) at the School of Earth Science and Geological Engineering of Sun Yat-sen University, Guangzhou, China. *In-situ* trace element analysis of magnetite was performed by laser ablation-inductively coupled plasma-mass spectrometry (LA-ICP-MS) at the Key Laboratory of Marine Resources and Coastal Engineering, Sun Yat-sen

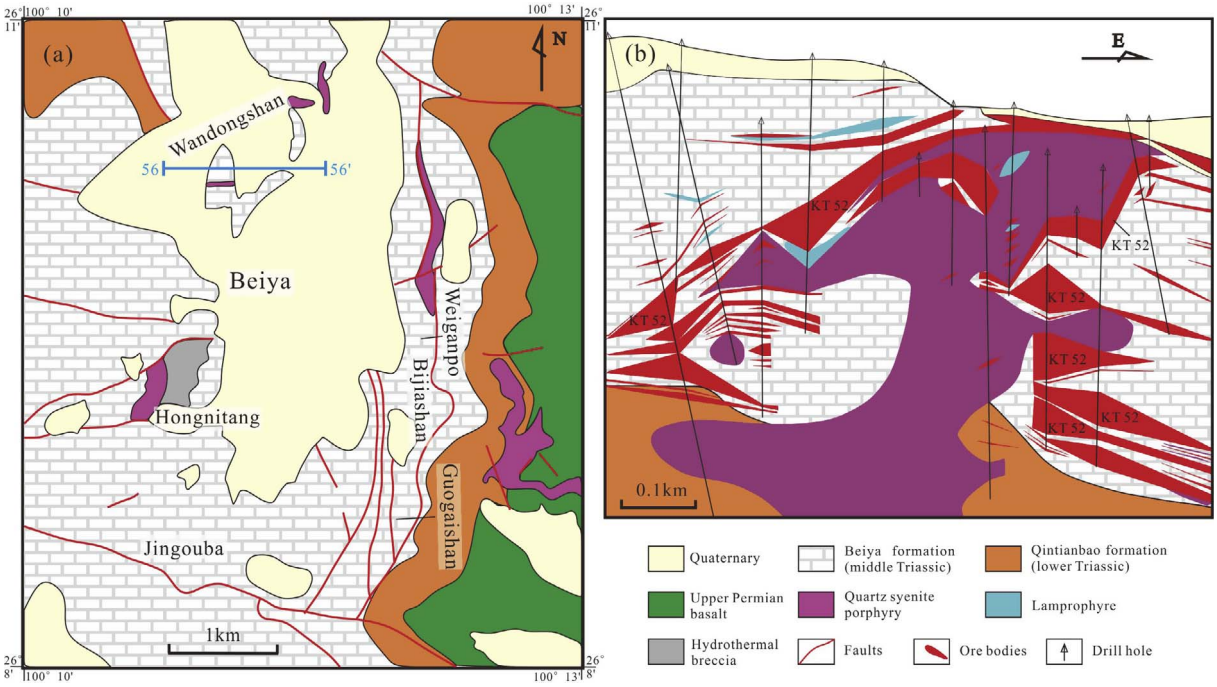

Fig. 2. Geologic map of the Beiya area (a) and the No.56 prospecting line cross section of the Wandongshan ore segment (b) (Modified after Lu et al., 2013; Xu et al., 2007).

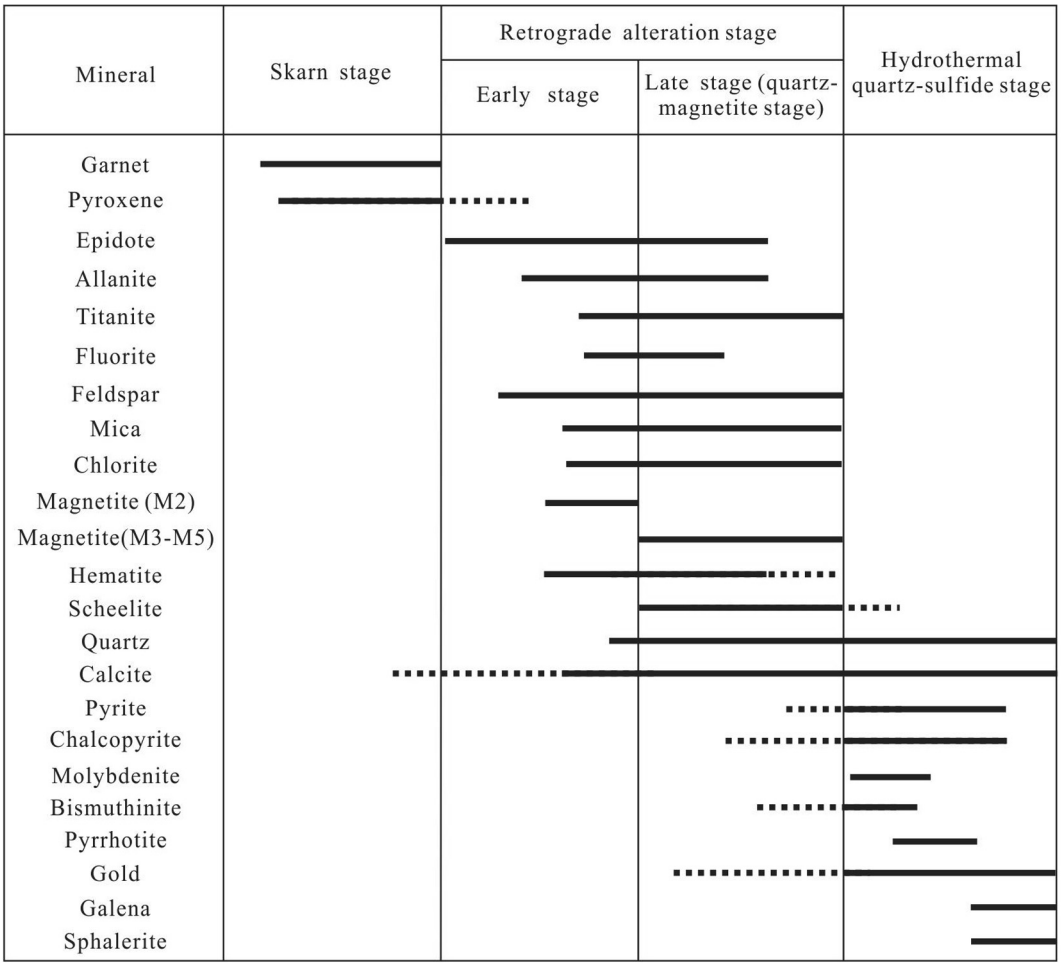

Fig. 3. Mineral paragenesis of the Beiya skarn mineralization.

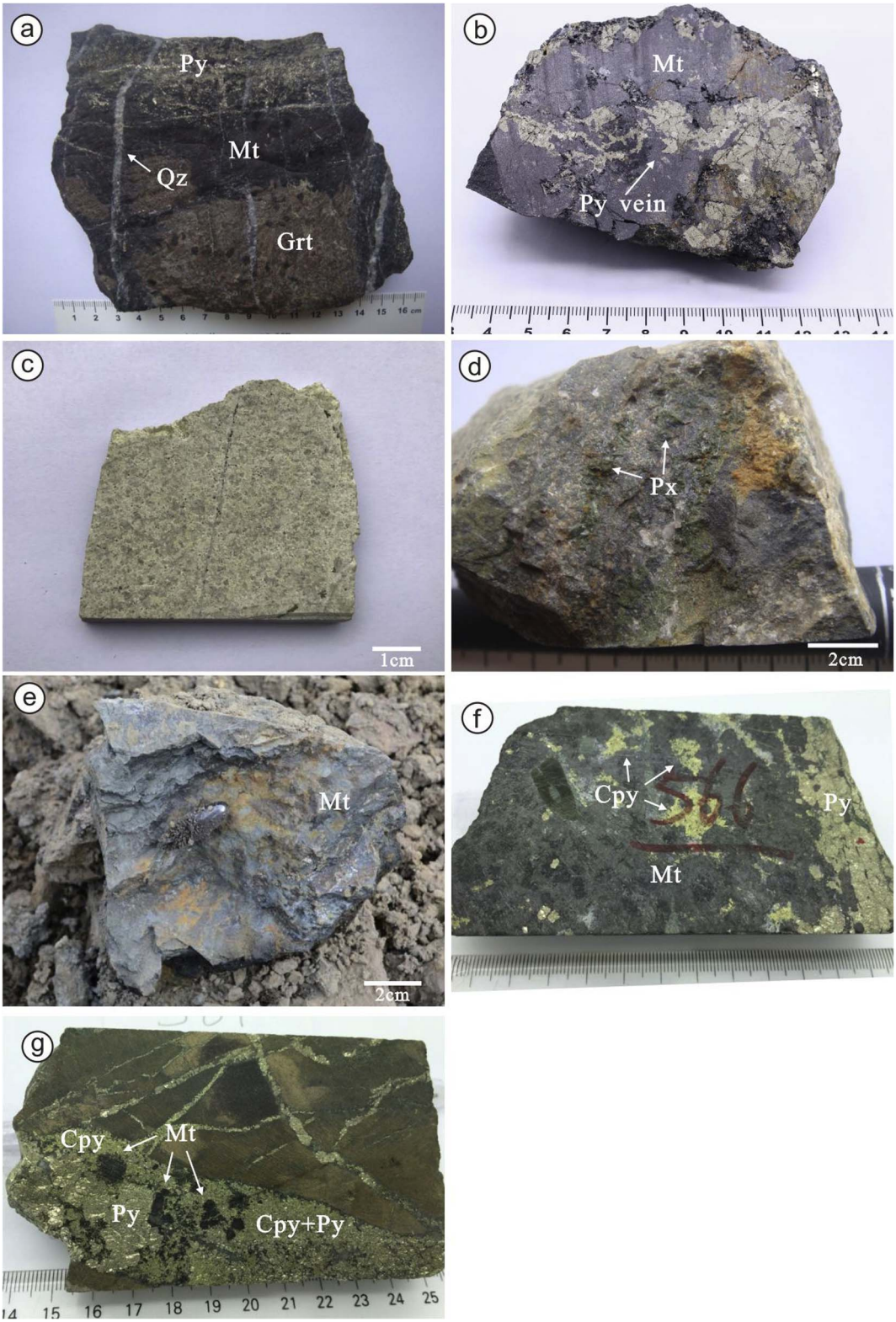

Fig. 4. Photographs of hand-specimens from the Beiya deposit showing mineralogy and textures of the five samples used in this study. (a) Typical skarn mineralization of the Beiya deposit. The early garnet was replaced by late magnetite, and the magnetite was then cut by the pyrite veinlets; (b) Magnetite ore cut by pyrite veins; (c) The ore-related quartz syenite porphyry collected from the open pit (M1); (d) Skarn with green pyroxene from the early retrograde alteration stage (M2); (e) Fe-oxide ore from the open pit dominated by massive magnetite with no sulfide (M3); (f) Massive magnetite ore coexisting with minor pyrite and chalcopyrite (M4); (g) Sulfide-dominated vein hosted within altered country rock, with minor magnetite coexisting with sulfides (M5). Abbreviations: Cpy-chalcopyrite, Grt-garnet, Mt-magnetite, Px-pyroxene, Py-pyrite, Qz-quartz.

University. The analysis was performed using an ArF excimer (193 nm) laser ablation system (GeoLasPro), and ion-signal intensities were acquired using an Agilent 7700x ICP-MS. A 32 μm spot was used with an energy density of 8 J/cm^2 and a repetition rate of 5 Hz. The trace element compositions of magnetite were calibrated against the USGS synthetic basalt glass GSE-1G, using Fe determined by electronic

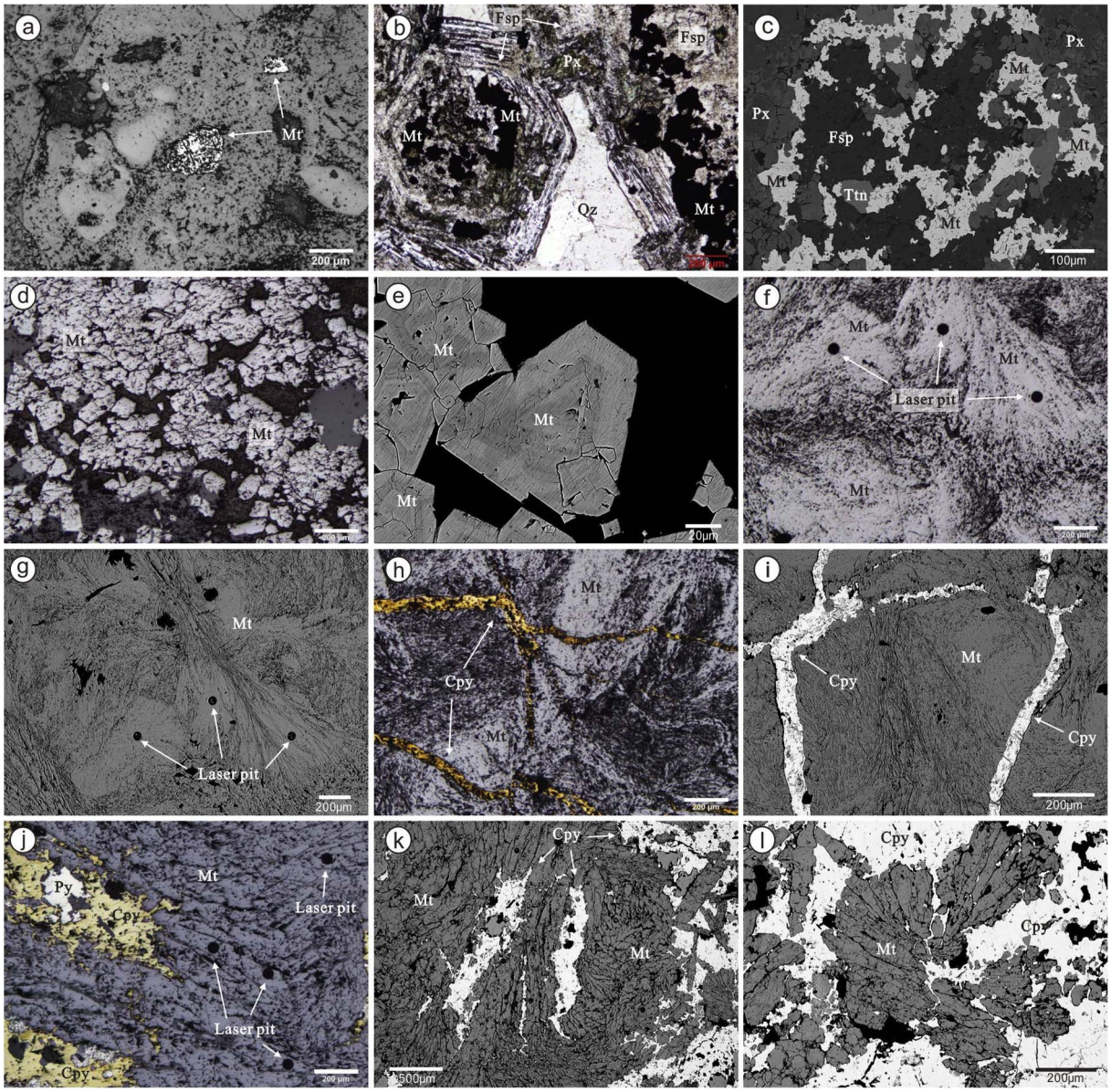

Fig. 5. Photomicrographs and BSE images of the magnetite samples from the Beiya deposit. (a) euhedral to subhedral magnetite grains in the ore-related porphyry (M1, reflected light); (b–c) magnetite in early retrograde alteration stage (M2, plane-polarized light and BSE respectively); (d) photomicrographs showing the occurrence of euhedral to subhedral magnetite grains in early quartz-magnetite stage (M3, reflected light); (e) BSE image of magnetite in W009; (f–g) magnetite in late quartz-magnetite (-sulfide) stage (M4, reflected light and BSE respectively); (h–i) magnetite cut by the chalcopyrite veinlets in M4 (reflected light and BSE respectively); (j-l) magnetite in early quartz-sulfide stage coexisting with large amounts of sulfide (M5, j: reflected light; k and l: BSE images). Abbreviations: Cpy-chalcopyrite, Fsp-feldspar, Mt-magnetite, Px-pyroxene, Qz-quartz, Ttn-titanite.

microprobe (EPM) as the internal standard. Each analysis consisted of a 20 s background measurement (laser-off) followed by 45 s data acquisition. Data reduction was performed using the ICPMSDataCal software (Liu et al., 2010). The international standard BC-28 (massive magnetite from the Bushveld intrusion; Dare et al., 2012) was used to monitor the data quality by analyzing it as an unknown sample. The values of Fe in magnetite were determined using a JEOL JXA-8800R EPM at the Instrumental Analysis & Research Center of Sun Yat-sen University. Operating conditions were 20 kV accelerating voltage and 20 nA beam current with a beam diameter of 2 μm.

The M1 grains in the porphyry are 50–100 μm in size and euhedral to subhedral with a rough surface. They occur as discrete grains in the interstices of magmatic minerals such as feldspar, biotite and quartz (Fig. 5a). M2 grains in the early retrograde alteration stage are mostly anhedral and intergrown with titanite, allanite and feldspar (Fig. 5b, c). They typically replace the skarn minerals (garnet) and occur in the cores and mantles of the garnet (Fig. 5b, c). In the early quartz-magnetite stage, M3 occurs as euhedral to subhedral crystals with sizes ranging from 50 to 200 μm (Fig. 5d, e). The M4 from the middle quartz-magnetite stage occurs as needle-like or fine-grained crystals (M4a; Fig. 5f, g), some of which are associated with minor sulfide minerals (chalcopyrite and pyrite) or are cut by chalcopyrite veinlets (M4b; Fig. 5h, i), suggesting that the sulfides began to form in this stage. M5 in the late quartz-magnetite stage is typically massive and associated with abundant chalcopyrite and pyrite (Fig. 5j–l). The grains of magnetite occur as euhedral to subhedral elongate crystals ranging from 50 to 500 μm in length. More sulfides formed in this stage than in the middle quartz-magnetite stage. In parts of the samples, the cracks and fractures in magnetite are filled by chalcopyrite, suggesting that they predate the precipitation of abundant sulfides in the following quartz-sulfide stage (Fig. 5l). BSE imaging did not reveal any overgrowth texture in the magnetite samples although some grains of W009 display patchy zoning (Fig. 5e), suggesting a single mineral growth phase in this study. All the analyses were performed on the homogeneous surfaces of the

Table 1
Summary of LA-ICP-MS results for trace elements (in ppm) in magnetite from the Beiya deposit.

Sample No.		Mg	Al	Si	Ca	Sc	Ti	V	Cr	Mn	Co	Ni	Zn	Ga	Ge	Sr	Nb	Sn	Ba	Hf	Th
M1	ave (n = 22)	605	5092	16689	1280	3.14	2104	1501	661	188	0.53	32.6	84.9	32.1	13.7	8.88	8.45	2.58	13.8	13.4	18.9
	stdev	281	2227	5888	1422	1.70	1297	103	923	51.8	0.50	6.2	30.2	4.06	3.48	3.95	6.55	1.81	7.38	32.0	16.1
M2 rim	ave (n = 5)	2322	3761	19490	3654	2.16	2053	588	71.0	1878	69.9	76.8	276	62.0	8.27	4.07	1.37	7.15	6.57	0.32	0.36
	stdev	1004	1438	5915	845	1.20	319	28	30.0	228	5.33	14.9	57.4	10.1	4.19	2.05	0.67	5.3	8.04	0.14	0.09
M2 core	ave (n = 12)	865	1420	13211	7538	4.49	288	524	189	1641	69.9	76.5	134	36.7	5.30	4.89	0.39	3.00	3.50	0.46	1.08
	stdev	412	530	3656	4047	2.19	129	12.6	69.7	126	2.87	10.0	20.5	5.23	1.26	2.27	0.25	2.95	2.39	0.32	0.44
M3	ave (n = 27)	270	339	10548	499	1.04	227	33.0	70.9	171	1.56	7.23	23.4	24.5	191	16.7	1.12	2.07	6.72	0.41	0.39
	stdev	135	133	1313	515	0.78	120	19.6	88.5	25.6	0.90	3.50	6.20	2.20	25.2	5.58	1.19	1.61	2.34	0.81	0.48
M4a	ave (n = 12)	117	150	2934	468	0.65	5.26	4.89	7.36	101	2.01	2.74	11.7	19.6	40.4	3.63	0.96	9.10	2.64	0.31	0.07
	stdev	35.3	60.7	1281	373	1.02	5.32	1.77	5.61	27.3	0.52	1.06	2.92	1.42	14.0	2.28	0.51	9.60	1.46	0.60	0.15
M4b	ave (n = 18)	87.6	121	2376	214	0.48	33.7	13.6	10.7	51.9	0.47	4.73	10.6	22.9	36.6	1.97	3.47	9.14	2.07	0.13	0.03
	stdev	85.6	8.04	647	373	0.43	17.6	2.83	5.67	39.6	0.26	1.93	4.94	0.83	2.76	0.56	0.53	5.08	0.55	0.36	0.07
M5	ave (n = 14)	275	513	3167	2030	1.89	27.5	38.2	4.32	795	0.29	4.20	31.0	33.1	58.2	7.10	2.16	87.4	3.46	0.03	0.03
	stdev	330	408	1589	1719	2.23	13.2	39.1	2.04	1472	0.26	2.30	14.7	2.70	26.0	3.87	2.85	95.9	2.78	0.07	0.02

Notes: ave-average, stdev-standard deviation.

magnetite grains identified in the BSE images.

4. Results

Results of LA-ICP-MS analysis for the different stages of magnetite at Beiya are presented in Appendix A. The average values and standard deviations of trace element contents in magnetite are listed in Table 1. The trace element data show that M1 magnetite is significantly enriched in Ti, V and Al compared with those of M2–M5 with average concentrations of 2104 ppm, 1501 ppm and 5092 ppm, respectively (Fig. 6a–c). M1 also has higher Sc, Cr, Nb, Hf and Th (average: 3.14 ppm, 661 ppm, 8.45 ppm, 13.4 ppm and 18.9 ppm, respectively) than its mineralized skarn counterpart (average: 1.55 ppm, 55.5 ppm, 1.67 ppm, 0.28 ppm, and 0.31 ppm, respectively; Fig. 6d–h).

The magnetite grains from different mineralization – alteration stages show distinct concentrations for most elements. M2 has higher Mg (average: 1294 ppm), Al (average: 2109 ppm), Ti (average: 807 ppm), V (average: 543 ppm), Mn (average: 1711 ppm), Co (average: 69.9 ppm), Ni (average: 76.5 ppm), and Zn (average: 176 ppm), and lower Ge (average: 6.17 ppm) than the other skarn samples (Fig. 6a–c, i–n). The Ti abundance is significantly lower in the magnetite that replaced garnet cores (M2 core/W364c: average of 288 ppm) than in the rim (M2 rim/W364r: average of 2053 ppm). M4 is characterized by low concentrations of Mg (average: 101 ppm), Al

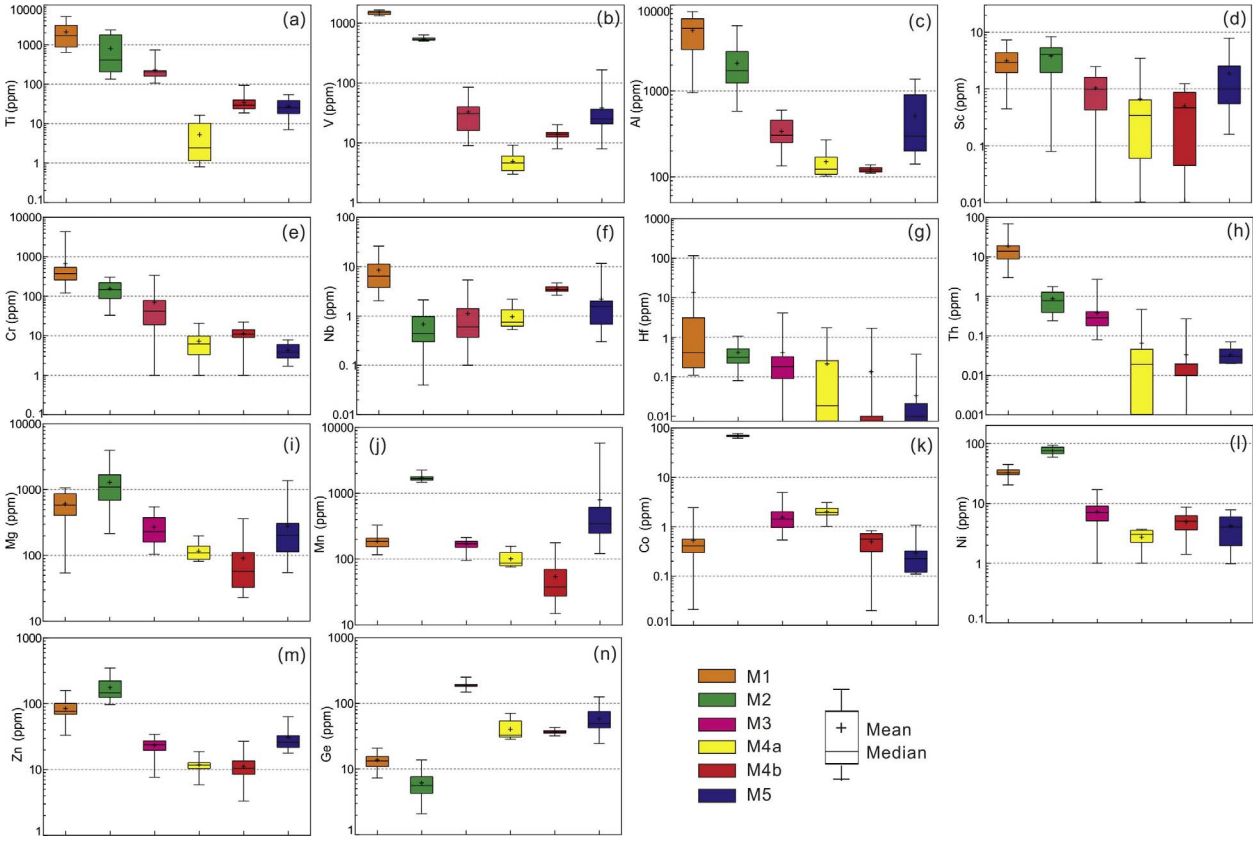

Fig. 6. Box and whisker plots of trace elements in magnetite from the Beiya deposit.

(average: 133 ppm), Sc (average: 0.56 ppm), Ti (average: 22.8 ppm), V (average: 10.3 ppm), Mn (average: 72.7 ppm) and Zn (average: 11.3 ppm) (Fig. 6a–d, i–j, m). Notably, M4 magnetite cut by chalcopyrite (M4b/W566b) contains lower Co (average: 0.50 ppm) and higher Ti (average: 34.5 ppm) and V (average: 13.9 ppm) than M4 not associated with sulfide minerals (M4a/W566a; average values of 2.01 ppm, 5.26 ppm and 4.89 ppm respectively; Fig. 6a–b, k). The M3 are enriched in Ge (148-251ppm average 191ppm), compared to other samples (Fig. 6n). Of all the trace elements, Cr and Co are consistently lower in M5 magnetite with concentrations of 1.69–7.91 ppm (average: 4.32 ppm) and 0.11–1.07 ppm (average: 0.29ppm), respectively (Fig. 6e, k).

5. Discussion

5.1. Genesis of magnetite

Magnetite can be sourced from either silicate melts or hydrothermal fluids (Dare et al., 2014). At the Beiya deposit, the magnetite from the Beiya ore-related porphyry (M1) belongs to the magmatic process and is analogous to igneous magnetite in terms of both mineralogy and geochemistry: M1 occurs as discrete grains in the interstices of igneous minerals (feldspar and quartz phenocrysts; Fig. 5a), suggesting a magmatic origin characterized by high Ti and V relative to those of hydrothermal magnetite, and Ti concentrations up to 5000 ppm which are consistent with published data for magmatic magnetite (Nadoll et al., 2015) (Fig. 7a). Moreover, M1 magnetites all plot in the field of igneous magnetite in Fig. 7b.

The magnetite in the Beiya mineralized samples (M2–M5) commonly co-precipitated with retrograde altered minerals (e.g., titanite, allanite and feldspar) and/or sulfide minerals (e.g., pyrite and chalcopyrite), suggesting a hydrothermal origin. The M2–M5 magnetites are depleted in Al, Sc, Ti, V, Nb and Hf (Table 1), consistent with hydrothermal magnetite (e.g., Nielsen and Beard, 2000; Dare et al., 2014). As shown in Fig. 7a and b, most M2–M5 samples plot in the hydrothermal field.

5.2. Element behavior in magnetite during the skarn forming process

The compositions of hydrothermal magnetite are generally considered to be governed by many factors including composition of the ore forming fluids; physicochemical parameters of ore fluids such as temperature, pressure, cooling rate, oxygen fugacity, sulfur fugacity, and silica activity; fluid-host rock interaction; and the co-crystallizing minerals (Chen et al., 2015a; Dare et al., 2014; Dupuis and Beaudoin, 2011; Huang et al., 2016; Nadoll et al., 2014, 2012). Although the abundance of each element could be influenced by more than one factor, some elements show regular changes between the magnetite from different ore forming stages in the Beiya deposit, and can be used to track and distinguish different stages of magnetite and the physicochemical changes during the skarn formation process.

Cobalt is a siderophile element and Fe sulfides can compete for it more effectively than oxides. Consequently, magnetite grains precipitated from a Co-rich fluid would have low Co concentrations if they are associated with sulfides (Acosta-Góngora et al., 2014; Dare et al., 2012). M4 grains cut by chalcopyrite (M4b) have lower Co contents (0.11–1.07 ppm) than the magnetites not associated with sulfides (M4a; 1.01–3.08 ppm) and shows a trend of increasing Co with distance from the chalcopyrite vein in M4b (Fig. 8a). The variation of Co in the magnetite from all the other retrograde alteration stages in this study also follows this pattern. In Fig. 8b, the concentrations of Co in magnetite decrease gradually from the M2 to M5 magnetites, which is consistent with the genetic model whereby the sulfides gradually increased in the ore forming system. In the M4 and M5 grains from the middle and end of the quartz-magnetite stage, Co is compatible in the Fe-rich sulfide solution resulting in Co-depletion in the co-crystallizing Fe oxide (Dare et al., 2012); conversely, the M2 and M3 magnetites not associated with sulfides have higher Co contents. In a sulfur-deficient system (early retrograde alteration stage), magnetite coprecipitates with trace amounts of sulfides and it will favor the partitioning of Co into the magnetite. In contrast, in the late retrograde alteration stage Co is more compatible with the sulfides, resulting in the Co depletion in magnetite (Acosta-Góngora et al., 2014). As the Co content in magnetite shows close relationship with ore forming stage (Co content decreased gradually from the early to the late stages; Fig. 8b), it can be used to distinguish the ore forming stages of the skarn mineralization.

Oxygen fugacity is an important factor that governs element behavior and possibly influenced Au segregation during the ore-forming process. Previous studies indicate that the behavior of V can be used to estimate the relative oxygen fugacity during the ore forming process (Nadoll et al., 2014, 2015 and references therein). The oxidation state of V in magnetite varies from 3+ to 5+. Among these species, V^{3+} has the highest compatibility with magnetite and consequently is the dominant cation in magnetite (Acosta-Góngora et al., 2014; Canil et al., 2016 and references therein). The valence state of V is very sensitive to the oxygen fugacity variation and even a small increase in fO_2 could

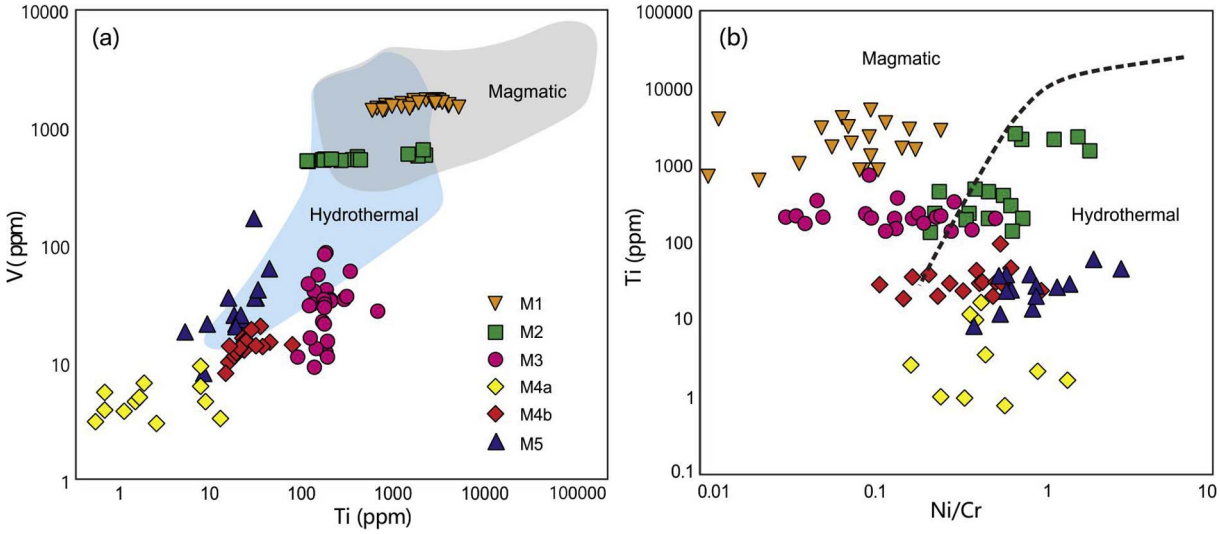

Fig. 7. Plots of Ti versus V (a) and Ni/Cr versus Ti (b) in magmatic and hydrothermal magnetite from the Beiya deposit. (Fields of magmatic and hydrothermal magnetite are from Dare et al. (2014) and Nadoll et al. (2015).

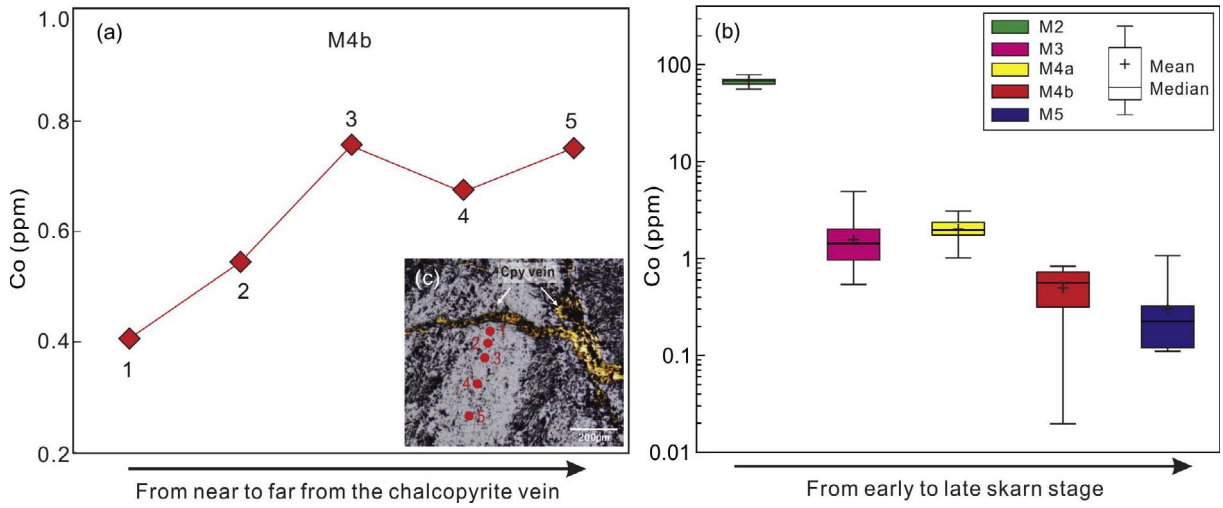

Fig. 8. Co distribution in magnetite from M4b (a) and different skarn stages (b) in the Beiya deposit. The locations of point 1 to point 5 in M4b are shown in (c).

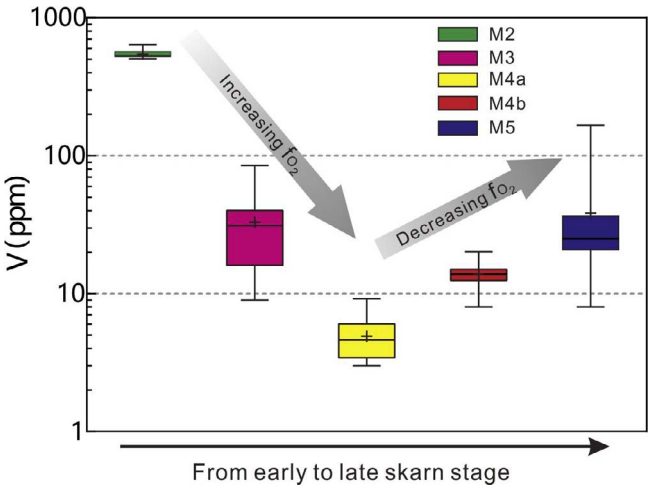

Fig. 9. Vanadium distribution in magnetite from different skarn stages in the Beiya deposit showing the oxygen fugacity changes in the ore-forming fluid.

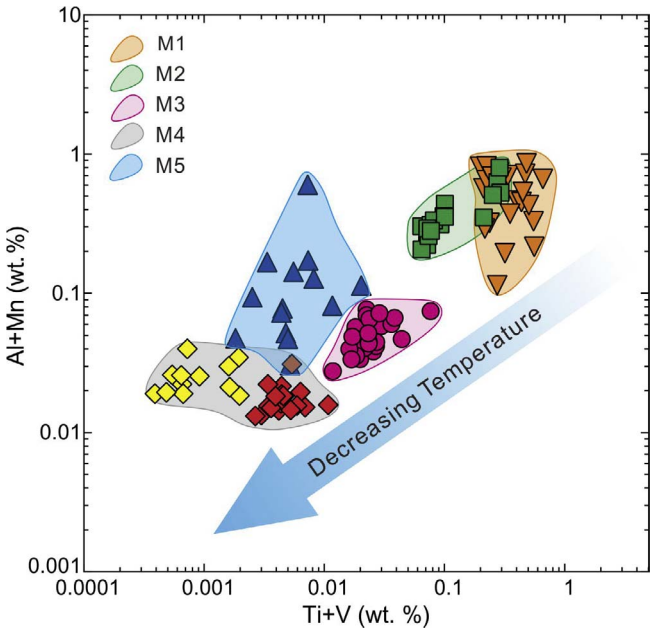

Fig. 10. Ti + V versus Al + Mn plots of magnetite in Beiya showing the temperature changes in the ore-forming process.

convert V^{3+} to V^{4+}, which is less compatible with the magnetite structure (Acosta-Góngora et al., 2014). Thus, the distributions of V between samples can reflect fO_2 differences in the ore-forming fluid with depletion in V reflecting an increase in fO_2. The V contents in magnetite of the Beiya deposit initially decrease and then increase from stages M2 to M5 (Fig. 9), which suggests that the fO_2 of the fluid increased within the early retrograde alteration stage, early quartz-magnetite stage to middle quartz-magnetite stage (M2–M4a), which contain minor to no sulfide, and then decreased from the middle quartz-magnetite stage (M4b) to the late quartz-magnetite stage (M5), resulting in the reduction of magnetite and the increase of sulfides in the samples.

Temperature is another major factor that could govern the partitioning behavior of trace elements into magnetite during the ore-forming process (McIntire, 1963; Nadoll et al., 2014). The concentrations of Ti in magnetite in hydrothermal systems is controlled by temperature (Canil et al., 2016). Previous studies have shown that the solubility of Al and Ti in the magnetite structure reflects a positive temperature dependence (Hu et al., 2015; O'Neill and Navrotsky, 1984). Additionally, V may not only be controlled by oxygen fugacity, but also by temperature in hydrothermal settings (Acosta-Góngora et al., 2014; Canil et al., 2016), consistent with the positive correlation between V and Ti contents in the magnetite from the Beiya deposit (Fig. 7). Nadoll et al. (2014) showed a Ti + V versus Al + Mn plot where data points were linked with temperature (Fig. 10). The diagram indicates that decreasing formation temperatures are reflected in the chemistry of the magnetite, with high temperature samples plotting at high Ti + V and Al + Mn whereas low temperature magnetite plot at low Ti + V and Al + Mn values. It can be seen in Fig. 10 that for magnetite from the M2 to M4 stages the temperature decreases gradually, consistent with cooling of the magma during the skarn mineralization process. The increase in Ti + V and Al + Mn values from M4 to M5 indicates that the temperature of the system increased. There is evidence of multiple porphyry intrusions at Beiya, consistent with previous research that has shown that skarn mineralization can be related to multiple pulses of igneous activity (e.g., Talate Zn-Pb (-Fe) skarn deposit; Li et al., 2014). The higher temperatures preserved in M5 magnetites may be the result of an influx of new magma into the chamber. As mentioned above, several alkaline porphyries were emplaced at Beiya area during ca. 36.9–33.3 Ma, indicating that the magma was emplaced in different stages with little crystallization age variations, which confirm the multiple magmatic emplacements. Similar processes have been invoked to account for the triggering of mineralization in other porphyry systems (Hattori and Keith, 2001; Hollings et al., 2013)

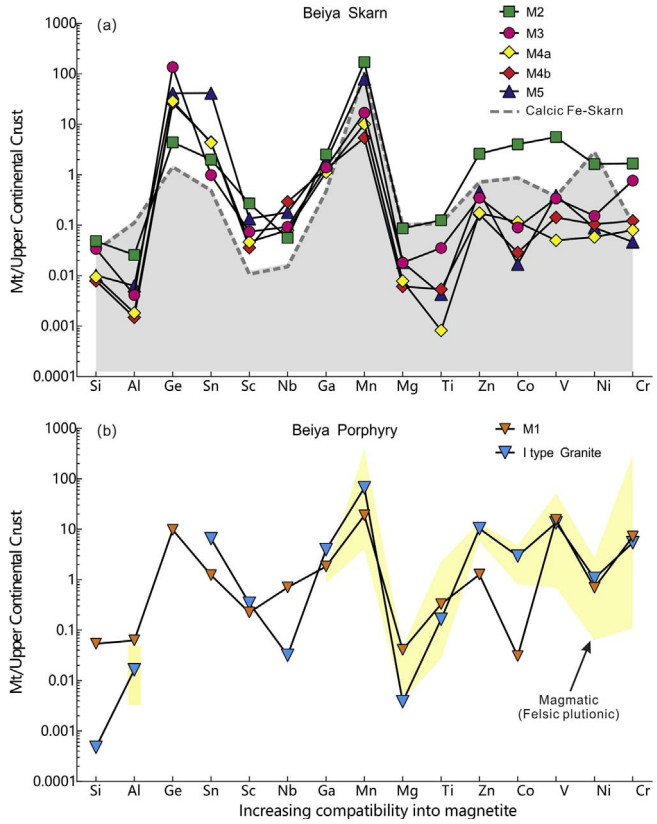

Fig. 11. Multielement variation diagrams for Beiya magnetite in the porphyry (a) and skarn (b), normalized to upper continental crust (values from Rudnick and Gao (2003)).

and may have triggered the Beiya gold polymetallic mineralization.

5.3. Implications for ore genesis

The chemical composition of magnetite varies between mineral deposit types (Dare et al., 2014; Dupuis and Beaudoin, 2011; Hu et al., 2015, 2014; Huang et al., 2016; Nadoll et al., 2014). For example, the multielement variation diagram for trace elements in magnetite can be applied to genetic and provenance studies of the ore deposit (Dare et al., 2014; Dupuis and Beaudoin, 2011; Nadoll et al., 2014). Magnetite from the retrograde alteration (including the Fe-oxide ores) and sulfide ores have patterns, similar to those of magnetite in calcic Fe-skarn deposits from Vegas Peledas, Argentina (Fig. 11a; Pons et al., 2009), but distinct from magnetite in the Beiya porphyry which is similar to magmatic accessory magnetite from felsic plutonic rocks and I-type granites (Dare et al., 2014 and references therein; Fig. 11b). Most of the hydrothermal magnetite from the Beiya deposit plot in the field of skarn in the discriminant diagrams developed by Dupuis and Beaudoin (2011) and Nadoll et al. (2015) (Fig. 12a, b), which implies that M2-5 are of hydrothermal origins from the skarn deposit, consistent with the conclusion discussed above.

Magnetite from Beiya plot in the BIF, IOCG and undefined fields or on the boundaries between these fields on discriminant diagrams (Fig. 12c). This scatter could be caused by a number of factors: (1) the discriminant diagrams introduced by Dupuis and Beaudoin (2011) were established by comparing a number of ore deposits and separating the average magnetite composition of one deposit from all other deposit types and as such do not reflect the true variation of magnetite in each deposit type; (2) Trace elements in magnetite can be modified by dissolution, re-precipitation and re-crystallization processes (Hu et al., 2015), which causes difficulties in using this mineral as a genetic indicator; (3) The geochemical signature of magnetite could be highly variable, due to regional and local variations in temperature, redox conditions, and trace element budgets in fluids and host rocks (Acosta-Góngora et al., 2014). This study suggests that trace elements in magnetite from skarn deposit might be more variable than previously thought, as proposed by Huang et al. (2013) and Zhao and Zhou (2015), suggesting that caution should be exercised when using these discriminant diagrams.

The Beiya hydrothermal magnetite from different mineralization stages show regular elemental distributions during the ore forming process. In the skarn stage, minerals are almost anhydrous and there is no magnetite. Magnetite mineralization mainly occurred during the retrograde alteration stage. M2 in the early retrograde alteration stage is characterized with high Ti, V, Co and Al + Mn contents, indicating the high temperature and low fO_2 environment. In the early and middle quartz-magnetite stages (M3 and M4), the Ti, V, Co and Al + Mn contents decreased with the decreasing temperature and the increasing fO_2, and the sulfide minerals occurred in the system. Then from the middle to late quartz-magnetite stages (M4 to M5), the Ti, V and Al + Mn contents increased, which suggests that the fO_2 decreased and the new magma was involved.

We propose that the M1 magnetite, which is characterized by high Ti (up to 5000 ppm) and V relative to those of hydrothermal magnetite (M2-5) formed during magma crystallization. The emplacement of the magma led to form skarn and driving the hydrothermal fluid along weak zones or fractures, cementing them with low grade magnetite, epidote and titanite. Increasing oxygen fugacity increased the metal carrying capacities within the hydrothermal fluids as tracked by V contents in the M2 to M4a magnetites, leading to deposition of large volumes of massive magnetite, which peaked during M4a. Subsequently, the fluid temperature increased likely the result of the influx of new magma before gradually decreasing in the quartz-sulfide stage. The gradually decreasing fO_2 and increasing of fS_2 from M4 to M5 is consistent with the switch from precipitation of magnetite to sulfides.

6. Conclusions

Magnetite grains from the Beiya deposit can be divided into five types, the magmatic magnetite (M1), and hydrothermal magnetite including the early retrograde alteration (M2), the early quartz-magnetite (M3), the middle quartz-magnetite (M4) and the late quartz-magnetite (M5) stages. The large volume of massive magnetite in Beiya ores are of hydrothermal origins from skarn deposit and distinct from the magmatic accessory magnetite in the ore-related porphyry (M1). The Co content in Beiya hydrothermal magnetite can be used to distinguish the ore forming stages of the skarn mineralization. The variation of V content and Ti + V versus Al + Mn values in Beiya magnetite reflects the changes in oxygen fugacity (increase from M2 to M4 and decrease from M4 to M5) and temperature (decrease from M2 to M4 and increase from M4 to M5) of the mineralizing fluids during the skarn ore forming process. The sudden changes in temperature from M4 to M5 may suggest an influx of new magma into the system that triggered the precipitation of gold from the ore forming fluid.

Acknowledgements

This work was jointly funded by the National Natural Science Foundation of China (Grant No. U1302233, 41602067, 41672071, 40830425, 40673045, 40873034), China Postdoctoral Science Foundation (No. 2015M582457), National Key Basic Research Program (Grant No. 2015CB452604, 2009CB421006; Ministry of Science and Technology, China), Higher School Specialized Research Fund for the Doctoral Program Funding Issue (Grant No. 200805580031), and the

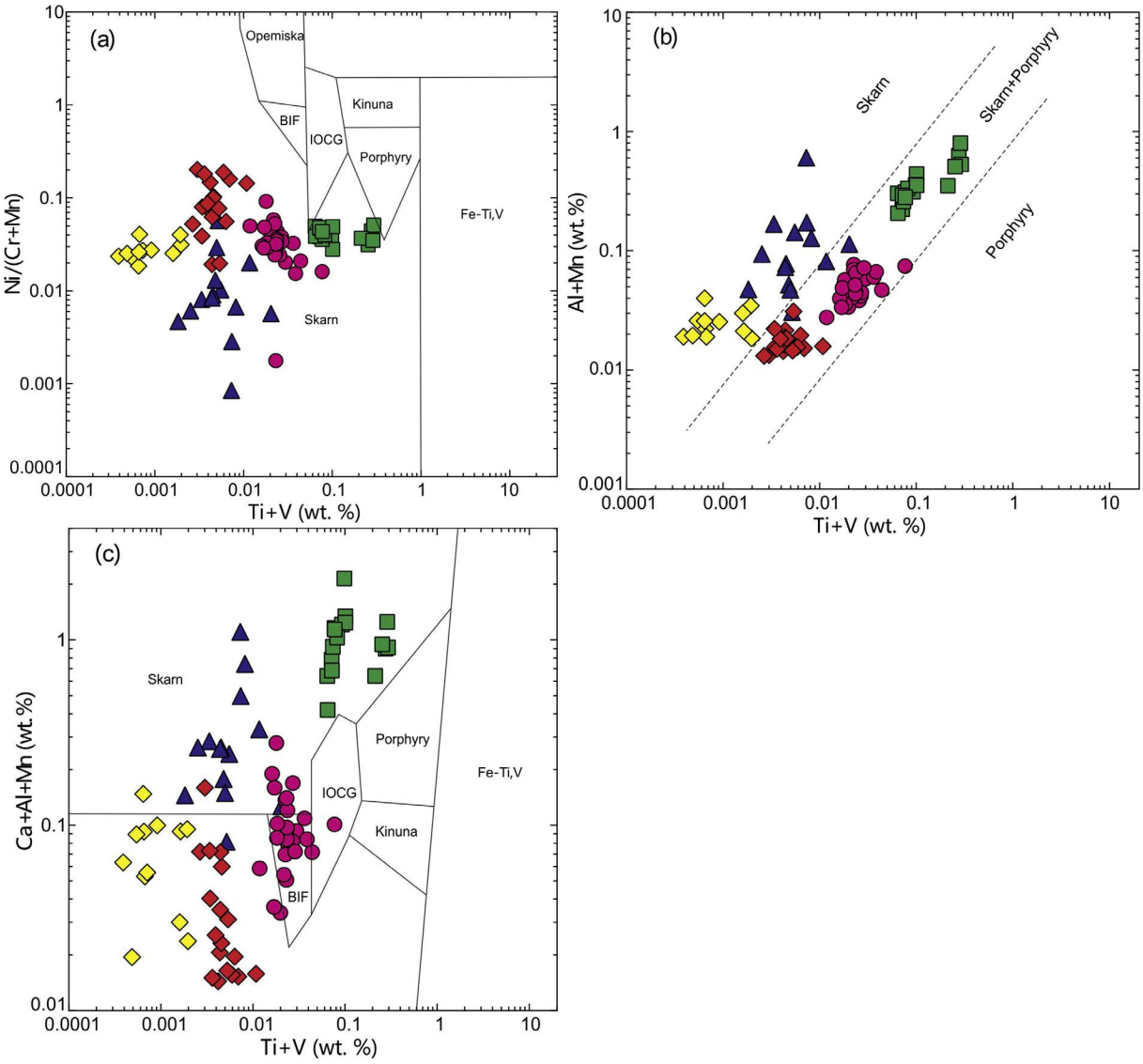

Fig. 12. Discriminant diagrams of (a) Ti + V versus Ni/(Cr + Mn) (Dupuis and Beaudoin, 2011), (b) Ti + V versus Al + Mn (Nadoll et al., 2015), and (c) Ti + V versus Ca + Al + Mn (Dupuis and Beaudoin, 2011) for magnetite from the Beiya deposit. The legend is the same as in Fig. 7.

Project Supported by Guangdong Province Universities and Colleges Pearl River Scholar Funded Scheme (Grant No. 2011). Dr. Wenchang Li is thanked for his kind support during our field work and sampling. The manuscript greatly benefited from the valuable comments and suggestions from Prof. Franco Pirajno, Editor-in-chief of Ore Geology Reviews, Prof. Jingwen Mao, Associate Editor of Ore Geology Reviews, and two anonymous reviewers.

Appendix A. Analytical results (in ppm) for LA-ICP-MS of magnetite from the Beiya deposit

Sample No.	Mg	Al	Si	Ca	Sc	Ti	V	Cr	Mn	Co	Ni	Zn	Ga	Ge	Sr	Nb	Sn	Ba	Hf	Th
W007 (M1)																				
01	426	2980	9529	1944	4.63	880	1489	400	217	0.30	44.7	60.1	29.7	14.2	14.4	6.76	3.26	15.9	0.17	48.9
02	511	5504	17174	1024	5.26	714	1401	4335	187	0.59	44.1	70.3	31.8	13.9	6.62	3.65	0.68	11.0	116	25.9
03	1066	7078	16959	2536	2.73	1304	1542	356	308	0.45	36.0	76.7	32.6	16.1	13.3	8.62	0.76	13.5	0.13	18.2
04	632	6931	24832	–	3.85	1739	1640	526	126	0.38	31.2	159	33.6	15.6	11.4	10.8	2.00	17.2	51.4	17.4
05	911	7103	17378	1924	3.17	3031	1663	577	118	0.55	29.8	81.9	32.8	12.7	9.01	12.5	3.59	10.3	0.44	12.9
06	980	7913	27436	–	4.55	637	1344	1550	194	0.35	34.5	120	34.9	15.5	7.41	6.08	–	8.59	0.27	6.33
07	808	8416	24603	1273	4.33	3192	1636	321	148	0.02	24.1	145	37.8	9.95	15.4	26.1	4.48	31.3	20.0	47.6
08	999	4489	15791	–	1.83	2335	1658	348	167	0.11	34.2	73.0	40.7	11.0	7.02	19.2	4.22	7.01	0.11	7.48
09	602	6298	16915	52.3	2.61	847	1390	369	172	0.55	32.9	76.4	24.6	12.7	6.30	4.96	0.54	13.0	3.12	8.33
10	884	7951	23259	800	7.31	870	1370	414	204	0.30	37.6	74.2	31.9	15.2	6.97	3.80	6.51	13.2	0.37	15.0
11	559	4326	12919	3262	3.06	2764	1611	154	210	0.28	39.9	72.7	31.9	9.87	5.56	4.07	3.86	11.4	0.36	19.0
12	297	2808	8215	6152	0.54	822	1345	331	116	0.13	33.2	47.0	23.3	19.0	6.20	7.42	1.87	9.08	0.17	9.54

13	54.2	951	8554	429	2.77	1288	1456	376	191	0.42	38.2	33.0	33.5	20.7	7.55	2.04	0.83	10.7	0.14	12.1
14	158	1754	10848	–	1.99	1679	1503	201	184	0.53	30.7	50.8	35.3	20.8	7.89	2.89	–	11.2	0.12	18.0
15	350	3066	10949	747	0.45	4029	1473	1842	221	0.65	23.9	94.3	38.0	13.9	6.38	4.25	3.62	9.80	1.15	8.98
16	271	1824	8569	312	0.94	4062	1512	458	327	2.43	31.5	74.2	32.0	7.31	5.69	2.14	5.69	5.83	0.84	3.00
17	855	6598	23267	2404	2.50	1575	1404	175	182	0.34	32.4	98.8	28.5	15.5	8.58	6.12	2.63	11.7	0.82	11.9
18	549	4113	12427	899	3.72	3468	1576	267	190	0.31	32.6	65.7	29.9	11.6	5.67	7.96	3.94	7.21	0.17	7.44
19	626	6486	18616	636	2.61	5157	1439	234	142	0.43	23.8	95.8	33.1	12.4	7.82	14.7	2.72	16.5	3.24	19.2
20	761	6728	22361	1312	3.41	1029	1457	804	170	0.53	30.8	110	27.7	11.9	21.1	7.25	1.41	36.5	2.12	19.9
21	484	3529	18385	875	1.22	1947	1565	393	208	1.33	30.6	107	32.2	10.6	5.72	3.39	1.37	13.0	0.35	10.2
22	516	5177	18177	1588	5.53	2921	1558	121	156	0.67	20.5	81.0	30.0	10.7	9.36	21.3	2.86	19.4	93.9	68.7
W364r (M2)																				
01	2174	4352	18442	2683	2.46	2173	584	74.7	1934	67.9	88.6	318	57.3	13.7	2.75	2.11	11.8	1.78	0.25	0.34
02	1857	3571	20080	3810	0.55	2356	572	55.8	1726	76.9	91.0	264	57.9	7.49	3.04	1.78	11.8	20.6	0.47	0.43
03	2328	3281	18661	4396	2.23	1963	563	77.1	1807	62.4	58.9	232	56.6	2.08	4.29	0.94	2.45	3.71	0.27	0.47
04	1283	1843	11858	2875	1.71	1543	583	33.1	1675	70.2	63.0	214	58.0	8.62	2.71	0.44	0.57	1.01	0.15	0.24
05	3969	5756	28409	4507	3.87	2232	636	114	2246	72.0	82.4	350	80.1	9.46	7.56	1.56	9.09	5.79	0.46	0.30
W364c (M2)																				
01	1088	2495	17708	9022	5.82	452	555	237	1915	70.1	60.2	147	42.9	6.21	6.68	0.60	1.10	9.93	0.40	1.07
02	216	659	8158	5614	1.71	194	524	182	1567	74.6	66.6	116	34.8	5.94	1.49	0.35	3.22	1.01	0.19	0.39
03	972	1559	12523	3358	4.19	138	504	116	1477	67.7	79.0	97.5	39.0	4.36	4.61	0.04	–	4.69	0.22	0.73
04	1088	1437	14584	8495	4.86	238	531	296	1673	70.7	70.5	161	37.2	6.65	9.72	0.28	–	3.37	0.31	1.43
05	482	583	6668	2119	0.08	134	512	307	1484	69.7	69.1	139	29.2	3.82	2.93	0.32	2.16	1.40	0.08	0.40
06	276	1046	9099	6613	4.08	207	530	98.8	1532	66.3	76.8	112	29.4	4.40	2.05	0.33	3.84	1.40	0.80	1.15
07	1221	1403	13928	8982	6.67	402	524	148	1721	69.5	89.6	149	37.0	5.51	5.29	0.45	4.40	3.20	0.92	1.15
08	589	1795	16399	17894	8.39	458	526	156	1783	66.3	76.7	120	34.6	7.83	4.82	0.56	9.98	3.43	1.07	1.61
09	1334	1727	14862	6961	6.00	303	516	104	1614	66.7	69.0	166	41.5	4.09	4.61	0.19	1.72	3.11	0.27	0.78
10	821	1309	15415	3924	3.47	202	517	176	1611	74.5	85.9	134	40.6	5.51	3.65	0.18	–	1.98	0.41	1.06
11	1505	1856	17521	8885	4.19	488	521	229	1680	70.5	93.8	142	44.4	5.57	5.99	1.02	6.39	5.07	0.56	1.40
12	789	1176	11667	8594	4.37	242	529	213	1637	72.3	80.4	129	30.2	3.70	6.81	0.32	3.13	3.38	0.22	1.77
W009 (M3)																				
01	425	382	11779	349	1.13	212	85.3	339	201	1.30	10.9	34.3	25.0	181	9.43	1.36	1.35	4.48	0.07	0.34
02	269	277	10899	352	0.79	209	31.4	33.2	155	2.15	8.14	26.7	25.3	191	16.6	0.61	1.15	4.66	0.32	0.22
03	104	232	8581	364	1.24	214	41.3	127	151	1.14	6.73	23.9	23.1	148	11.4	2.27	2.15	3.98	0.12	0.47
04	489	463	11074	278	1.37	175	55.0	268	174	2.01	11.3	29.6	24.4	194	11.5	0.64	0.83	6.99	0.27	0.39
05	521	590	11320	602	0.99	213	12.2	8.66	176	1.52	4.51	30.1	26.0	193	28.3	0.26	0.51	10.8	0.12	0.56
06	273	441	9446	486	1.95	329	34.4	19.0	162	2.44	5.87	29.5	22.7	153	16.2	3.43	6.90	7.03	0.10	0.61
07	549	531	9216	266	0.70	741	26.8	42.1	214	1.54	4.12	22.3	23.4	170	12.3	5.35	2.50	5.14	0.03	0.41
08	206	269	9375	401	1.21	235	33.9	36.4	149	1.51	7.01	26.6	24.4	183	11.0	1.35	2.62	4.80	0.10	0.40
09	144	306	9421	246	2.29	381	59.1	27.8	164	2.83	4.02	28.1	25.3	183	22.7	1.65	3.80	8.57	0.16	0.46
10	200	196	10025	–	0.75	159	39.9	64.5	141	2.04	8.78	23.6	23.8	185	13.3	0.58	1.05	5.64	0.25	0.34
11	160	251	9929	68.2	2.01	220	11.4	9.51	187	0.96	0.35	7.65	25.2	159	26.5	0.48	–	9.06	0.67	0.09
12	186	277	10103	1241	2.00	237	33.5	96.0	170	4.94	9.05	16.6	21.4	183	11.6	1.18	2.15	6.79	4.12	0.41
13	257	498	11396	172	0.49	350	35.6	77.7	169	1.43	3.78	27.3	22.4	181	13.5	2.86	5.21	7.26	0.09	0.40
14	210	306	12757	392	1.62	220	15.0	19.9	143	0.71	5.13	26.4	24.6	251	26.7	0.37	2.29	9.91	0.19	0.26
15	377	343	10366	2251	0.05	167	12.9	–	184	2.31	16.9	27.2	22.0	247	9.25	0.27	–	3.27	0.41	0.16
16	160	261	9552	135	0.43	195	22.4	60.5	145	1.03	11.9	20.6	25.2	202	21.8	0.83	2.15	10.4	–	0.30
17	230	363	12115	284	0.32	151	31.0	53.5	208	1.89	7.58	21.3	25.4	238	19.0	0.46	1.60	6.25	0.18	0.16
18	173	266	10043	535	–	201	33.5	58.8	170	0.75	8.23	33.4	24.3	195	14.8	0.66	0.80	5.57	0.29	0.25
19	382	600	12160	–	1.36	204	20.8	29.7	95.0	1.35	6.57	26.5	28.4	194	21.6	0.23	2.37	9.39	0.06	0.21
20	374	456	13106	552	2.33	206	30.7	47.7	198	0.54	8.44	18.2	27.3	199	19.6	0.56	2.84	8.12	1.54	2.71
21	190	184	11122	666	1.37	138	46.5	63.2	172	0.96	7.74	25.1	25.1	188	14.0	0.42	0.77	4.57	0.94	0.27
22	156	208	10462	1498	–	145	16.2	15.9	190	0.54	6.27	19.6	28.0	194	19.8	0.31	2.22	8.87	0.13	0.29
23	262	308	10154	1106	–	141	30.2	34.5	180	1.20	10.3	21.9	24.5	185	14.2	0.64	3.01	4.53	0.21	0.17
24	515	536	12297	–	2.48	205	82.4	290	185	0.72	–	14.6	29.0	195	9.82	1.42	0.17	6.71	0.05	0.24
25	241	319	11224	886	0.58	204	28.9	91.3	197	1.52	9.21	19.9	25.3	214	20.6	1.74	3.97	10.5	0.33	0.18
26	117	134	7917	308	0.71	107	10.8	–	142	1.18	7.10	15.7	19.3	153	14.1	0.10	0.45	2.82	–	0.08
27	122	155	8943	26.9	–	160	9.07	–	181	1.73	5.24	15.4	21.4	189	21.1	0.18	3.14	5.23	0.32	0.13
W566a (M4a)																				
01	83.0	104	1762	52.3	0.27	16.5	3.28	6.15	80.2	1.85	2.71	11.7	17.8	30.5	1.63	0.70	3.34	1.97	–	0.01
02	109	111	1883	440	0.25	0.76	3.14	3.19	79.1	1.94	1.94	11.4	19.0	28.4	2.13	0.88	4.21	3.22	1.35	0.02
03	109	106	1576	703	0.09	3.52	3.04	4.76	116	2.06	2.24	12.0	19.2	32.5	2.69	0.73	2.92	1.71	–	0.06
04	199	102	1558	634	–	1.65	3.78	2.58	157	1.71	3.70	12.7	19.0	32.8	2.75	0.89	4.67	1.82	0.01	0.05
05	80.6	110	2133	340	0.39	2.14	4.58	3.58	80.1	1.99	3.40	12.4	18.4	30.6	2.16	0.67	3.70	1.79	0.17	0.01
06	155	135	2855	715	0.05	10.2	6.20	13.5	76.0	1.50	–	10.0	19.4	33.6	2.47	1.56	2.87	1.90	0.02	0.09

07	86.2	270	5873	606	0.49	10.2	9.16	8.21	76.2	2.27	3.38	11.4	21.9	70.9	9.32	1.48	26.3	6.40	–	0.02
08	128	269	4255	157	3.48	2.28	4.99	–	130	3.08	3.54	9.53	19.8	52.0	6.16	0.59	30.3	3.39	–	–
09	97.4	170	3164	–	1.83	11.5	4.56	9.15	130	2.39	3.51	18.6	21.5	55.7	3.66	2.18	14.1	4.00	1.78	0.52
10	143	142	3202	746	0.70	2.58	6.55	20.7	111	2.49	3.61	5.89	17.4	31.5	2.95	0.80	4.69	1.29	0.04	–
11	119	111	3243	–	0.28	0.95	3.90	6.37	83.2	1.84	2.27	13.5	20.1	31.8	2.04	0.53	2.78	1.41	0.36	–
12	90.3	168	3701	1219	–	1.00	5.45	10.1	89.8	1.01	2.61	11.5	21.1	54.1	5.62	0.53	9.31	2.75	0.00	–
W566b (M4b)																				
01	43.1	117	2052	–	0.25	29.3	12.6	9.09	27.1	0.41	5.33	13.5	23.9	35.3	1.74	4.09	13.0	1.89	–	0.01
02	101	121	1477	418	0.13	30.7	15.2	13.9	59.2	0.54	7.54	8.71	23.3	37.8	2.16	3.34	12.2	2.36	0.02	0.01
03	52.2	126	3066	44.2	–	29.4	14.3	11.3	35.6	0.75	3.26	13.8	23.9	34.3	1.57	3.33	25.2	1.77	–	–
04	32.0	118	2553	1463	0.06	20.1	9.93	9.42	14.9	0.67	4.92	9.34	23.1	37.5	1.66	3.47	6.94	2.62	–	0.01
05	215	110	3787	135	1.00	28.3	15.9	21.3	105	0.75	2.43	10.7	22.7	39.8	2.58	4.18	7.39	2.42	0.57	0.02
06	124	114	2783	529	0.54	29.3	14.9	12.2	73.3	0.64	5.35	7.68	23.0	36.3	2.77	3.26	15.9	2.34	–	0.01
07	48.1	119	2730	248	0.40	23.1	11.2	10.8	36.3	0.72	3.75	8.97	22.6	37.8	1.18	3.07	10.4	1.40	–	0.01
08	79.3	127	2890	47.8	1.25	30.6	14.9	15.9	56.5	0.58	7.24	9.09	23.2	35.4	2.11	3.53	5.57	1.54	–	0.01
09	61.0	111	1908	–	–	24.2	12.0	9.00	39.1	0.68	8.68	11.1	22.4	36.6	1.68	3.18	6.64	2.58	–	0.07
10	107	128	2628	–	0.83	43.3	20.1	10.4	68.0	0.02	4.35	14.2	24.1	32.0	2.05	4.32	7.78	2.14	1.44	0.10
11	33.4	120	2966	–	0.77	54.5	14.7	–	32.2	0.10	5.14	7.58	23.8	35.2	1.58	3.83	11.2	1.69	–	0.27
12	32.5	128	1793	–	–	45.7	13.5	11.0	27.6	0.40	7.28	5.26	23.3	40.2	1.69	2.93	10.4	1.23	0.03	0.01
13	28.7	123	2836	19.0	0.34	38.8	13.7	12.4	22.8	0.32	2.71	26.8	23.8	33.7	1.99	2.62	5.03	2.17	–	–
14	65.7	114	2244	73.2	1.03	26.2	13.1	–	68.7	0.83	5.95	13.6	21.8	35.4	1.80	3.08	10.2	1.53	–	–
15	23.4	114	2950	587	1.10	18.7	7.98	9.04	17.7	0.78	1.40	3.33	21.3	35.0	1.33	3.68	5.89	1.77	0.35	0.04
16	181	138	2050	507	–	20.5	13.6	15.3	83.4	0.30	3.84	11.2	21.5	37.0	2.55	3.52	4.36	2.95	–	–
17	360	134	1126	–	0.68	34.9	18.8	22.2	177	0.36	3.92	10.2	23.3	42.7	3.42	4.67	5.66	2.41	–	0.02
18	54.2	130	2180	–	0.68	94.1	14.0	9.20	27.5	0.11	5.27	13.0	22.9	41.3	2.33	3.25	5.62	3.23	–	0.01
W561 (M5)																				
01	107	855	1516	129	7.90	37.3	166	2.90	283	0.11	1.63	62.3	35.1	24.7	2.57	11.6	366	2.54	0.02	0.07
02	309	1373	2602	1167	1.41	12.1	21.4	2.75	304	0.30	2.48	63.7	33.2	42.0	4.28	0.59	125	4.19	–	0.02
03	303	1046	4569	3256	4.98	38.8	34.8	3.07	674	0.55	1.93	41.5	35.0	75.2	12.9	1.71	220	5.42	–	0.05
04	274	1065	6918	1000	3.98	20.1	35.3	4.03	362	0.27	3.75	29.9	36.9	126	14.3	0.75	70.1	11.4	–	0.02
05	54.6	265	1694	980	0.30	10.7	7.62	1.69	210	1.07	0.99	26.3	26.9	36.9	3.56	0.26	93.1	1.14	0.06	0.05
06	132	259	2029	1261	0.16	23.3	24.6	2.69	260	0.27	3.42	21.9	33.7	42.5	3.69	1.60	37.4	1.45	–	0.03
07	201	311	2388	1859	0.60	23.8	21.1	6.94	469	0.18	4.32	26.1	31.1	47.2	5.93	1.19	35.4	2.55	0.25	0.02
08	202	427	3619	2481	1.26	54.4	62.4	3.82	388	0.40	7.87	23.3	37.4	63.0	6.82	3.46	40.2	2.59	0.01	0.03
09	116	286	2506	1023	0.68	26.7	23.1	3.75	185	0.29	5.52	25.0	33.6	49.1	4.98	1.52	46.2	2.24	0.02	0.02
10	1376	204	3831	5040	2.06	38.1	34.7	5.74	5831	0.12	4.96	29.7	30.8	75.9	10.4	1.92	29.2	3.08	–	0.05
11	336	145	2371	6158	0.80	40.9	41.0	2.56	1130	0.15	7.59	26.1	31.1	48.5	8.44	2.27	15.0	1.45	0.01	0.03
12	69.2	185	1984	510	0.53	27.0	24.9	7.91	121	0.18	7.36	19.1	31.9	43.5	3.46	1.26	48.3	1.35	0.02	0.02
13	243	141	2634	1858	0.56	24.0	19.9	7.86	588	0.12	4.97	21.4	32.8	51.1	6.10	1.75	30.7	2.43	–	0.04
14	130	618	5673	1693	1.19	7.50	17.7	4.76	320	0.11	1.97	17.7	33.6	89.1	11.9	0.38	68.2	6.56	0.02	0.02

Notes: "–" means the content of the element is below detection limit.

References

Acosta-Góngora, P., Gleeson, S.A., Samson, I.M., Ootes, L., Corriveau, L., 2014. Trace element geochemistry of magnetite and its relationship to Cu-Bi-Co-Au-Ag-U-W mineralization in the great bear magmatic zone, NWT. Canada. Econ. Geol. 109, 1901–1928.

Canil, D., Grondahl, C., Lacourse, T., Pisiak, L.K., 2016. Trace elements in magnetite from porphyry Cu-Mo-Au deposits in British Columbia, Canada. Ore Geol. Rev. 72, 1116–1128.

Chen, W.T., Zhou, M.F., Gao, J.F., Hu, R., 2015a. Geochemistry of magnetite from Proterozoic Fe-Cu deposits in the Kangdian metallogenic province, SW China. Miner. Depos. 50, 795–809.

Chen, W.T., Zhou, M.F., Li, X., Gao, J.F., Hou, K., 2015b. In-situ LA-ICP-MS trace elemental analyses of magnetite: Cu-(Au, Fe) deposits in the Khetri copper belt in Rajasthan Province, NW India. Ore Geol. Rev. 65, 929–939.

Chung, D., Zhou, M.F., Gao, J.F., Chen, W.T., 2015. In-situ LA-ICP-MS trace elemental analyses of magnetite: The late Palaeoproterozoic Sokoman Iron Formation in the Labrador Trough, Canada. Ore Geol. Rev. 65, 917–928.

Dare, S.A.S., Barnes, S.J., Beaudoin, G., 2012. Variation in trace element content of magnetite crystallized from a fractionating sulfide liquid, Sudbury, Canada: Implications for provenance discrimination. Geochim. Cosmochim. Acta 88, 27–50.

Dare, S.A.S., Barnes, S.J., Beaudoin, G., Méric, J., Boutroy, E., Potvin-Doucet, C., 2014. Trace elements in magnetite as petrogenetic indicators. Miner. Depos. 49, 785–796.

Deng, J., Wang, Q., Li, G., Hou, Z., Jiang, C., Danyushevsky, L., 2015. Geology and genesis of the giant Beiya porphyry-skarn gold deposit, northwestern Yangtze Block, China. Ore Geol. Rev. 70, 457–485.

Dupuis, C., Beaudoin, G., 2011. Discriminant diagrams for iron oxide trace element fingerprinting of mineral deposit types. Miner. Depos. 46, 319–335.

Fu, Y., Sun, X., Lin, H., Zhou, H., Li, X., Ouyang, X., Jiang, L., Shi, G., Liang, Y., 2015. Geochronology of the giant Beiya gold-polymetallic deposit in Yunnan Province, Southwest China and its relationship with the petrogenesis of alkaline porphyry. Ore Geol. Rev. 71, 138–149.

Fu, Y., Sun, X., Zhou, H., Lin, H., Yang, T., 2016. In-situ LA-ICP-MS U-Pb geochronology and trace elements analysis of polygenetic titanite from the giant Beiya gold-polymetallic deposit in Yunnan Province, Southwest China. Ore Geol. Rev. 77, 43–56.

Fu, Y., Sun, X., Zhou, H., Lin, H., Jiang, L., Yang, T., 2017. In-situ LA-ICP-MS trace elements analysis of scheelites from the giant Beiya gold-polymetallic deposit in Yunnan Province, Southwest China and its metallogenic implications. Ore Geol. Rev. 80, 828–837.

Hattori, K.H., Keith, J.D., 2001. Contribution of mafic melt to porphyry copper mineralization: evidence from Mount Pinatubo, Philippines, and Bingham Canyon, Utah, USA. Miner. Depos. 36, 799–806.

He, W.Y., 2014. The Beiya giant gold-polymetallic deposit: magmatism and metallogenic model. China University of Geosciences (Beijing).

He, W., Yu, X., Mo, X., He, Z., Li, Y., Huang, X., Su, G., 2012. Genetic type and the relationship between alkali-rich intrusion and mineralization of Beiya gold-polymetallic ore field, western Yunnan Province, China. Acta Geol. Sin. 28, 1401–1421.

He, W., Mo, X., Yu, X., He, Z., Dong, G., Liu, X., Su, G., Huang, X., 2013. Zircon U-Pb and molybdenite Re-Os dating for the Beiya gold-polymetallic deposit in the western Yunnan Province and its geological significance. Acta Petrol. Sin. 29, 1301–1310.

He, W., Mo, X., He, Z., White, N.C., Chen, J., Yang, K., Wang, R., Yu, X., Dong, G., Huang, F., 2015. The geology and mineralogy of the Beiya skarn gold deposit in Yunnan, Southwest China. Econ. Geol. 110, 1625–1641.

He, Z.H., Guan, D.R., He, W.Y., Zhou, Y.M., Fu, D.G., Yang, S., Wang, L., Li, W.H., Su, G.S., Yang, R., 2016. Exploration moldel of Beiya superlarge gold-polymetallic

deposit, northwestern Yunnan. Miner. Depos. 35, 261–282.
Hollings, P., Sweet, G., Baker, M., Cooke, D., Friedman, R., 2013. Tectonomagmatic controls on porphyry mineralization: Geochemical evidence from the Black Mountain porphyry system, Philippines. Soc. Econ. Geol. Spec. Publ. Number 17, 301–335.
Hu, H., Li, J., Lentz, D., Ren, Z., Zhao, X., Deng, X., Hall, D., 2014. Dissolution-re-precipitation process of magnetite from the Chengchao iron deposit: Insights into ore genesis and implication for in-situ chemical analysis of magnetite. Ore Geol. Rev. 57, 393–405.
Hu, H., Lentz, D., Li, J., Mccarron, T., Zhao, X., Hall, D., 2015. Reequilibration processes in magnetite from iron skarn deposit. Econ. Geol. 110, 1–8.
Huang, X., Zhou, M., Qi, L., Gao, J., Wang, Y., 2013. Re-Os isotopic ages of pyrite and chemical composition of magnetite from the Cihai magmatic-hydrothermal Fe deposit, NW China. Miner. Depos. 48, 925–946.
Huang, X., Gao, J., Qi, L., Meng, Y., Wang, Y., Dai, Z., 2016. In-situ LA-ICP-MS trace elements analysis of magnetite: The Fenghuangshan Cu-Fe-Au deposit, Tongling. Eastern China. Ore Geol. Rev. 72, 746–759.
Jiang, C., Wang, Q., Li, G., Ma, N., Hu, Z., 2013. Relative oxidation states of intrusions in Beiya gold-polymetallic deposit in Sanjiang area, Yunnan, SW China. Acta Geol. Sin. 29, 3925–3936.
Li, D., Zhang, L., Chen, H., Zheng, Y., Hollings, P., Wang, C., Fang, J., 2014. Ore genesis of the unusual Talate Pb–Zn(–Fe) skarn-type deposit, Altay, NW China: constraints from geology, geochemistry and geochronology. Geol. J. 49, 599–616.
Li, W., Wang, J., He, Z., Dou, S., 2016. Formation of Au-polymetallic ore deposits in alkaline porphyries at Beiya, Yunnan, Southwest China. Ore Geol. Rev. 73, 241–252.
Liu, Y., Gao, S., Hu, Z., Gao, C., Zong, K., Wang, D., 2010. Continental and oceanic crust recycling-induced melt-peridotite interactions in the Trans-North China Orogen: U-Pb dating, Hf isotopes and trace elements in zircons from mantle xenoliths. J. Petrol. 51, 537–571.
Liu, B., Liu, H., Zhang, C., Mao, Z., Zhou, Y., Huang, H., He, Z., Su, G., 2015. Geochemistry and geochronology of porphyries from the Beiya gold-polymetallic orefield, western Yunnan, China. Ore Geol. Rev. 69, 360–379.
Lu, Y., Kerrich, R., Cawood, P.A., McCuaig, T.C., Hart, C.J.R., Li, Z., Hou, Z., Bagas, L., 2012. Zircon SHRIMP U-Pb geochronology of potassic felsic intrusions in western Yunnan, SW China: Constraints on the relationship of magmatism to the Jinsha suture. Gondwana Res. 22, 737–747.
Lu, Y., Kerrich, R., Kemp, A.I.S., McCuaig, T.C., Hou, Z., Hart, C.J.R., Li, Z., Cawood, P.A., Bagas, L., Yang, Z., Cliff, J., Belousova, E.A., Jourdan, F., Evans, N.J., 2013. Intracontinental eocene-oligocene porphyry Cu mineral systems of Yunnan, Western Yangtze Craton, China: Compositional characteristics, sources, and implications for continental collision metallogeny. Econ. Geol. 108, 1541–1576.
Mao, J., Pirajno, F., Lehmann, B., Luo, M., Berzina, A., 2014. Distribution of porphyry deposits in the Eurasian continent and their corresponding tectonic settings. J. Asian Earth Sci. 79, 576–584.
Mao, J., Zhou, Y., Liu, H., Zhang, C., Fu, D., Liu, B., 2017. Metallogenic setting and ore genetic model for the Beiya porphyry-skarn polymetallic Au orefield, western Yunnan, China. Ore Geol. Rev. 86, 21–34.
McIntire, W.L., 1963. Trace element partition coefficients—a review of theory and applications to geology. Geochim. Cosmochim. Acta 27, 1209–1264.
Meinert, L., Hedenquist, J., Satoh, H., Matsuhisa, Y., 2003. Formation of Anhydrous and Hydrous Skarn in Cu-Au Ore Deposits by Magmatic Fluids. Econ. Geol. 98, 147–156.
Nadoll, P., Koenig, A.E., 2011. LA-ICP-MS of magnetite: methods and reference materials. J. Anal. At. Spectrom. 26, 1872.
Nadoll, P., Mauk, J.L., Hayes, T.S., Koenig, A.E., Box, S.E., 2012. Geochemistry of magnetite from hydrothermal ore deposits and host rocks. Econ. Geol. 107, 1275–1292.
Nadoll, P., Angerer, T., Mauk, J.L., French, D., Walshe, J., 2014. The chemistry of hydrothermal magnetite: a review. Ore Geol. Rev. 61, 1–32.
Nadoll, P., Mauk, J.L., Leveille, R.A., Koenig, A.E., 2015. Geochemistry of magnetite from porphyry Cu and skarn deposits in the southwestern United States. Miner. Depos. 50, 493–515.
Nielsen, R.L., Beard, J.S., 2000. Magnetite–melt HFSE partitioning. Chem. Geol. 164, 21–34.
O'Neill, H.S., Navrotsky, A., 1984. Cation distributions and thermodynamic properties of binary spinel solid solutions. Am. Mineral. 69, 733–753.
Pons, J., Franchini, M., Meinert, L., Recio, C., Etcheverry, R., 2009. Iron skarns of the Vegas Peladas District, Mendoza, Argentina. Econ. Geol. 104, 157–184.
Rudnick, R.L., Gao, S., 2003. Composition of the continental crust. Treatise Geochem. 3, 659.
Tooth, B., Ciobanu, C.L., Green, L., Neill, B.O., Brugger, J., 2011. Bi-melt formation and gold scavenging from hydrothermal fluids: an experimental study. Geochim. Cosmochim. Acta 75, 5423–5443.
Wang, J., Yin, A., Harrison, T.M., Grove, M., Zhang, Y., Xie, G., 2001. A tectonic model for Cenozoic igneous activities in the eastern Indo-Asian collision zone. Earth Planet. Sci. Lett. 188, 123–133.
Xiao, X., Yu, X., Mo, X., Li, Y., Huang, X., 2011. Geochemical characteristics of the metallogenesis in the gold-polymetallic deposit in Beiya, western Yunnan Province. Geol. Explor. 47, 170–179.
Xu, S., 2007. Metallogenic modeling of the Beiya gold deposit in western Yunnan and its relation to the Cenozoic alkali-rich porphries. China University of Geosciences (Beijing).
Xu, X., Cai, X., Song, B., Zhang, B., Ying, H., Xiao, Q., Wang, J., 2006. Petrologic, chronological and geochemistry characteristics and formation mechanism of alkaline porphyries in the Beiya gold district, western Yunnan. Acta Petrol. Sin. 22, 631–642.
Xu, X., Cai, X., Xiao, Q., Peters, S.G., 2007. Porphyry Cu-Au and associated polymetallic Fe-Cu-Au deposits in the Beiya Area, western Yunnan Province, south China. Ore Geol. Rev. 31, 224–246.
Xue, C., Hou, Z., Liu, X., Yang, Z., Liu, Y., Hao, B., 2008. Petrogenesis and metallogenesis of the Beiya gold-polymetallic ore district, northwestern Yunnan province, China: Responses to the Indo-Asian collisional processes. Acta Petrol. Sin. 24, 457–472.
Zhao, W., Zhou, M., 2015. In-situ LA-ICP-MS trace elemental analyses of magnetite: The Mesozoic Tengtie skarn Fe deposit in the Nanling Range, South China. Ore Geol. Rev. 65, 872–883.
Zhou, H., Sun, X., Fu, Y., Lin, H., Jiang, L., 2016. Mineralogy and mineral chemistry of Bi-minerals: Constraints on ore genesis of the Beiya giant porphyry-skarn gold deposit, southwestern China. Ore Geol. Rev. 79, 408–424.
Zhou, H., Sun, X., Cook, N.J., Lin, H., Fu, Y., Zhong, R., Brugger, J., 2017. Nano to Micron-Scale Particulate Gold Hosted By Magnetite: a Product of Gold Scavenging by Bismuth Melts. Econ. Geol. 112, 993–1010.